CrystEngComm

Accepted Manuscript

ROYAL SOCIETY OF CHEMISTRY

www.rsc.org/crystengcomm

Highly Crystalline Ti-doped SnO_2 Hollow Structured Photocatalyst with Enhanced Photocatalytic Activity for Degradation of Organic Dyes

Lei Ran, Longwei Yin*

Key Laboratory for Liquid-Solid Structural Evolution and Processing of Materials, Ministry of Education, School of Materials Science and Engineering, Shandong University, Jinan 250061, P. R. China

*To whom correspondence should be addressed. Tel.: + 86 531 88396970. Fax: + 86 531 88396970. E-mail: yinlw@sdu.edu.cn

Abstract We develop a facile infiltration route to synthesize hollow structured SnO_2 with an adjustable Ti doping content using SiO_2 microspheres as hard templates via an improved Stober method. The microstructures of the as-prepared Ti-doped SnO_2 samples were characterized by XRD, SEM, TEM, XPS, N_2 adsorption and desorption techniques. The photocatalytic activity of the hollow structured Ti-doped SnO_2 photocatalysts was investigated by decomposing Methylene Blue (MB) under UV and visible light illumination in a photochemical reactor. It is revealed that the hollow structured Ti-doped SnO_2 spherical specimens display enhanced photocatalytic activity toward decomposing MB than pure SnO_2 sample. In comparison with pure SnO_2 hollow spherical sample, Ti-doped SnO_2 with a doping content of 20 mol% displays the highest photocatalytic activity, with 92% MB photocatalytically decomposed under UV light irradiation, with 54% MB photocatalytically decomposed under visible light irradiation, within a degradation time of 135 min, respectively. The relation between microstructure, optical responsibility, photocatalytic performance is discussed and analyzed. The photocatalytic performance enhancement of Ti-doped SnO_2 can be attributed to the following reasons. Homogenous doping of Ti into lattice of SnO_2 prevents the recombination of the electron-hole pairs, and expands the range of useful excitation light to the visible light region. In addition, highly crystalline state, large surface area, and large pore size of the Ti-doped SnO_2 also contribute to the improved photocatalytic activity of the Ti-doped SnO_2 samples.

Keywords: tin dioxide; hollow spheres; doping; photocatalysis

1. Introduction

Along with the development of photocatalytic technology in recent years, it is gradually evolving an independent and prosperous field of study, which is expected to play a significant role in abatement of environmental pollutants, especially degradation of refractory organic pollutants,[1-3] including detergents, dyes, pesticides and herbicides. Nanoscale semiconductor has received extensive attention as a potential effective photocatalyst due to its unique effects,[4, 5] such as small dimension effect, quantum dimension effect, surface effect and macroscopical quantum tunnel effect. Among various semiconductor materials, TiO_2-based photocatalysts have been most thoroughly investigated and comprehensively employed in photocatalysis elimination of organic and inorganic compounds, owing to their high efficiency, chemical stability, low cost, non-toxicity, and photostability.[6-8] However, TiO_2 is active only under near-ultraviolet irradiation and no visible light response can be obtained due to its wide band gap energy of 3.2 eV. Moreover, the high recombination rate of photogenerated electron-hole pairs is also the main obstacle for enhancing the photocatalytic efficiency of TiO_2 for practical applications. Alternatively, as an archetypical n-type semiconductor, tin oxide (SnO_2) displays a variety of applications in gas sensor,[9] anode material for lithium ion battery,[10] transparent conductive electrode,[11] dye-sensitized solar cells,[12] photocatalysis,[13] photovoltaic conversion,[14] owing to its unique photoelectric effect, high chemical stability, excellent acid and alkali resistance. SnO_2 can cover a spectral bandwidth different from TiO_2 due to its peculiar energy-band structure. Furthermore, there is a coordination effect between SnO_2 and TiO_2 in the TiO_2/SnO_2 composite system for photocatalysis process. For instance, Levy et al.[15] investigated the photogenerated carriers transfer process in a double-layered TiO_2/SnO_2 heterostructured film prepared from a colloidal suspensions of TiO_2 deposited on a transparent layer of F-doped SnO_2 on glass, suppressing recombination of photogenerated carriers, showing an enhancement of photo quantum yield and photocatalytic activity.

However, the band gap of SnO_2 is wide (E_g = 3.62eV at room temperature) that it can be activated by UV light only, resulting in a low photocatalytic activity for SnO_2. The suppression of recombination of photogenerated electron-hole pairs before their participation in redox processes constitutes a key issue for improving the photocatalytic efficiency of corresponding photocatalyst.[16] One of the promising solutions is to introduce metal doping species to improve trapping behavior of electrons to inhibit electron-hole pair recombination, which can be attributed to the modification of band gap energy structure and introduction of dopant energy state. Due to the relation between ionic electronegativity and energy gap, substitution of Sn^{4+} by metallic ions in the SnO_2 lattice can create an allowed energy state in the band gap of SnO_2, and induce a photoactive transition in the visible light. Thus far, many ionic dopants in different valence states have been investigated, including both transition metallic ions (Zn,[16] Fe,[19] Co,[20] Mn,[21] Ni[20]) and nonmetal ions (F[22], N[23]), other type of ions (Ga[24]). Another effective route to decrease the recombination rate of photogenerated charges of electrons and holes is to combine SnO_2 with some noble metal nanoparticles, such as Ag,[25] Au,[26] Pt,[27] to form a semiconductor-metal heterostructure. Diverse structural and morphological forms of SnO_2 nanomaterials have been reported over the past several years, including nanoparticles,[28] nanowires,[29] hollow spheres,[30] nanobelts,[31] nanoribbons,[32] nanorods,[33] nanotubes,[34] nanodiskettes,[35] nanocomposites,[36] and thin films.[37] Specially, hollow structured materials with large surface area have been attracting much attention for their potential applications for their excellent adsorption ability to reactant molecules owing to their low density, high surface area, and porous structure.[38-40] So far, numerous preparation approaches have been reported to centrally prepare hollow structured spherical samples, such as self-assembly, soft- and hard-template, emulsion techniques, and so forth. Up to now, the photocatalytic performance on hollow SnO_2 spherical nanostructures with an adjustable doping concentration of Ti, with a light responsibility tuned, is almost seldom reported.

Herein, we develop a facile infiltration route to prepare hollow structured SnO_2 with an adjustable Ti doping content using SiO_2 microspheres as hard templates through improved Stober method. The microstructures of the prepared Ti-doped SnO_2 samples were characterized by XRD, SEM, TEM, XPS, N_2 adsorption and desorption. The photocatalytic activity of the hollow structured Ti-doped SnO_2 photocatalyst was tested by decomposing Methylene Blue (MB) illuminated under UV and visible light in a photochemical reactor. It is revealed that hollow structured Ti-doped SnO_2 spherical specimens display enhanced photocatalytic activity on MB than SnO_2 sample. Especially, Ti-doped SnO_2 with a doping content of 20 mol% displays the highest photocatalytic activity, with 92% and 54% MB photocatalytically decomposed under UV and visible light irradiation, within degradation time of 135 min, respectively. The relation between microstructure, optical responsibility, photocatalytic performance is discussed and analyzed.

2 Experimental section

2.1 Synthesis of SiO_2 microspheres and hollow structured Ti-doped SnO_2

In the improved Stober process[41] for synthesizing SiO_2 microspheres, 110 ml ethanol and 18 ml ammonium hydroxide (28 wt%) were put into a flat bottom flask with vigorous stirring. After 5 min, 7.5 g TEOS was added dropwise into the above homogeneous solution. Afterward, the mixture was stirred for 10 h at room temperature. Subsequently, the white precipitate product (2.08 g) was harvested by 3 centrifuge disperse-rinse cycles with DI water and then dried at 80 ℃.

The preparation process for hollow structured Ti-doped SnO_2 is described in following detail. 1.53 g of $SnCl_2•2H_2O$ was melted to liquid phase at 80 ℃. Then, 1.0 g of as-prepared SiO_2 microspheres was added under stirring after it was pre-heated at 100 ℃ for 1 h to completely remove water from the mesopores of the silica. Afterward, 5 mL of deionized water was added into the above mixture and was sonicated for 3-5 min to form a homogeneous sol, and a predetermined amount of tetrabutyl titanate was added. The final solution was put into an oven at 80 ℃ overnight to ensure the infiltration of tin precursor and titanium precursor on surface of SiO_2 microspheres. After the above reaction, the resulted light yellow solid product was kept in a tube furnace in air at 700 ℃ for 3 h, at a ramping rate of 3 ℃ min^{-1}. Then, in order to remove the silica, sodium hydroxide solution ($0.1 mol•L^{-1}$) was prepared by dissolving NaOH (2 g) in DI water (500 ml), then the product was dispersed in 50 ml NaOH solution with stirring, and heated to 50 ℃ and maintained at this temperature for 12 h. Before the separation procedure, the PH value of washings can be measured, the results are presented in Table 1. The as-fabricated product was collected by centrifugation, washed with DI water and ethanol, respectively, and then dried in an oven at 80 ℃ for 12 h. Finally, after drying process, a light grey powder was obtained. According to this method, the Ti-doped SnO_2 nanocomposites with different Sn : Ti molar ratios (10, 20 and 50 mol%) were fabricated and the as-obtained samples were labeled as SnO_2 (10%Ti)、SnO_2 (20%Ti) and SnO_2 (50%Ti), respectively. In addition, for comparison, pure SnO_2 sample was denoted as SnO_2. Furthermore, the yields of the obtained products can be calculated and shown in Table 1.

Table 1 The yields of the syntheses and PH value of washings

Samples	Theoretical output (g)	Actual output (g)	Yield (%)	PH of washings
SiO_2	2.16	2.08	96.22	
SnO_2	1.21	1.15	94.67	8.5
SnO_2 (10%Ti)	1.26	1.13	89.61	9.0
SnO_2 (20%Ti)	1.31	1.18	90.27	8.2
SnO_2 (50%Ti)	1.60	1.43	89.67	9.3

2.2 Structural characterization

Powder X-ray diffraction (XRD) patterns were recorded on a Philips Rigaku D/Max-KA X-ray diffractometer using a Cu Ka radiation source (λ = 1.54178Å) with an operation voltage and operation current being 40 kV and 50 mA, respectively. Field emission scanning electron microscope (FESEM: SU-70) was used to observe the morphology of samples. The high-resolution transmission electron microscopy (HRTEM) images were acquired using a JEM-2100 (acceleration voltage of 200 kV). Nitrogen adsorption–desorption isotherms were carried out at 77 K using a Gold APP V-Sorb 2800 surface area and porosity analyzer. The surface area measurements were performed according to the Brunauer–Emmett–Teller (BET) method. The pore size distribution was obtained from the desorption branch of the isotherm using the corrected form of the Kelvin equation by means of the Barrett–Joyner–Halenda (BJH) method. X-ray photoelectron spectroscopic (XPS) measurements were conducted on an ESCALAB 250 electron spectrometer using Al Kα radiation. XPS data were calibrated using the binding energy of C1s (284.7 eV) as the internal standard. UV-vis absorption spectra of the as-synthesized samples mixed with ethanol solution were measured with a TU-1901 double-beam UV-visible spectrophotometer. The photoluminescence (PL) spectra of photocatalysts were detected with recorded using conventional spectrometers (Hitachi U-4100 and Cary-50. Varian Co., respectively)

2.3 Photocatalyitc activity

Photocatalytic test was conducted on a XPA-7 photochemical reaction apparatus equipped with an internal light source (300 W Hg lamp and 350 W Xe lamp were used as UV light and visible light source) surrounded by a water-cooling quartz jacket to cool the lamp, where a 50 mL of the Methylene Blue (MB) solution with an initial concentration of 20 mg L^{-1} in the presence of solid catalyst (0.0125 g). The suspension was stirred in the absence of light for 60 min to obtain a good dispersion and reach an adsorption/desorption equilibrium between the organic dye molecules and the catalyst surface prior to irradiation. The solution was continuously stirred during the experiment. The concentration of MB in the centrifuged aqueous solution was determined by monitoring the absorption maximum of MB at λmax = 664 nm on TU-1901 double-beam UV-visible spectrophotometer. A calibration plot based on Beer–Lambert's law was established by relating the absorbance to the concentration.

3 Results and discussion

3.1 Structural characterization of hollow structured Ti-doped SnO_2

The crystalline structure and phase component of SnO_2 and Ti-doped SnO_2 were examined by X-ray powder diffraction

(XRD). Fig. 1 depicts typical wide-angle XRD patterns of the synthesized materials. Both pure and Ti-doped SnO_2 samples exhibit similar XRD patterns that can be indexed to rutile structure. All diffraction peaks in Fig. 1 are in good agreement with those of standard patterns for tetragonal rutile SnO_2 (JCPDS no. 41-1445) with a space group of P42/mnm and lattice constants of a = 4.74 Å, c = 3.19 Å. No other additional peaks are observed in the XRD patterns, confirming that both SnO_2 and Ti-doped SnO_2 are highly pure without any impurities. The diffraction peaks of the SnO_2 nanocrystals are sharp, indicating that the synthesized materials are highly crystalline. The diffraction peaks at 26.61, 33.89, 37.95, 51.78° can be well assigned to (110), (101), (200), (211) planes of rutile SnO_2, respectively. With the increase of Ti doping content into lattice of SnO_2, the XRD diffraction peaks display a right shift trend, maintaining well crystal structure of rutile SnO_2. The diffraction peak deviation trend of the Ti-doped SnO_2 samples can be further intuitively investigated. Fig. 1b depicts magnified XRD patterns of (110) and (101) planes with different Ti doping contents, clearly showing a right shift trend for the XRD peaks with the increase of Ti-doping content. This suggests that the Ti doping in SnO_2 causes the decrease of lattice constants due to the smaller diameter of Ti^{4+} than Sn^{4+}.

For the metal ion doping, there exists two types of modes. In the case of the interstitial mode, the ionic radius of dopant is smaller than that of the matrix metal ion, allowing the doped metal ions to enter the crystal cell of the matrix. Upon doping through the substitutional mode, the dopant will substitute the lattice metal ions and thus occupy the positions of the metal ions in the lattice of matrix. In order to thoroughly investigate the doping mechanism, the lattice constants of various Ti doping content of Ti-doped SnO_2 are calculated according to Brag equation by using the (101) diffraction peak of rutile SnO_2, and the results are summarized in Table 2. It can be seen that along with increasing Ti doping content in the range of 0-50 mol%, the lattice constants (a×c) of Ti-doped SnO_2 samples can be calculated to be 4.754×3.194, 4.737×3.184, 4.734×3.161 and 4.708×3.155, respectively. It can be indicated that Ti doping induces a decrease in lattice constants of SnO_2, which is likely correlated with the smaller ion radius of Ti^{4+} compared with that of Sn^{4+}. Because the radius of Ti^{4+} and Sn^{4+} ions is 60.5 pm and 69 pm,[42] respectively, the Ti^{4+} ion can easily replace the Sn^{4+} ion in the lattice of SnO_2 and forms a solid solution, without greatly changing the lattice constants of SnO_2 matrix, only causing a fluctuation in lattice constants of SnO_2.

Table 2 Unit cell parameters of SnO_2 and Ti-doped SnO_2 samples

Samples	*a* (Å)	*c* (Å)	V ($Å^3$)
SnO_2	4.754	3.194	71.76
SnO_2 (10%Ti)	4.737	3.184	71.47
SnO_2 (20%Ti)	4.734	3.161	71.17
SnO_2 (50%Ti)	4.708	3.155	71.10

The microstructure and surface area of the synthesized materials (SnO_2 and SnO_2 (20%Ti)) were further determined by the Brunauer–Emmett–Teller (BET) method at 77 K. The nitrogen adsorption and desorption isotherms and the corresponding pore size distribution curves of pure SnO_2 and Ti-doped SnO_2 samples are shown in Fig. 2. As revealed in the isotherms (Fig. 2a), a typical II cure with a hysteresis loop can be observed, indicating typical porous materials including macropores and mesopores. The hysteresis loop located in high relative pressure (P/P0 > 0.85) may be attributed to the space caused by the accumulation of particles. An estimation of the mean pore size can be obtained from 4V/A where V is the total pore volume and A the specific area. The mean pore sizes of SnO_2 and SnO_2 (20%Ti) are 45.8±0.5 nm and 60.7±0.5 nm, respectively. The textural properties including surface area, pore size and pore volume of all samples are listed in Table 3. With Ti doping content increasing, the surface area, specific pore volume, and pore size increase from 26.2±0.5 m^2 g^{-1}, 0.30±0.01 cm^3 g^{-1} and 45.8±0.5 nm for pure SnO_2 sample to 35.6±0.5 m^2 g^{-1}, 0.54±0.01 cm^3 g^{-1}, and 60.7±0.5 nm for Ti-doped SnO_2 (20%Ti) sample, respectively. It is generally accepted that the photocatalysis process is mainly related to the adsorption and desorption of molecules on the surface of photocatalyst.[43] A high specific surface area can facilitate electrons transfer and provide a sufficient amount of interface for photocatalysis reactions, resulting in enhanced photocatalytic activity.[44]

Table 3 The textural parameters of SnO_2 and 20%Ti-doped SnO_2 samples

Samples	Surface area / (m^2 g^{-1})	Pore size / (nm)	Pore volume / (cm^3 g^{-1})
SnO_2	26.2±0.5	45.8±0.5	0.30±0.01
SnO_2 (20%Ti)	35.6±0.5	60.7±0.5	0.54±0.01

XPS spectra were used to investigate the chemical bonding state through the binding energies and intensities of the elements. From an XPS survey spectrum (Fig. 3a) for the SnO_2 (20%Ti) sample, it is indicated that the sample is mainly composed of Ti, Sn, O elements. From XPS analysis, the actual atomic ratio for Ti:Sn is 1.98:7.99 for the 20%Ti-doped SnO_2. The XPS survey spectrum indicates the presence of silicon specie, which is attributed to the inevitably incompletely removed silica template. Fig. 3b-3d displays the high-resolution XPS spectra for the Sn 3d, O 1s and Ti 2P species, respectively. According to XPS result, Fig. 3b demonstrates that the peaks are located at 486.4 and 495.2 eV, which are ascribed to the Sn 3d 5/2 and Sn 3d 3/2 , respectively, indicating the valence state of Sn is +4. The lower value of the Sn 3d$_{5/2}$ binding energy for Ti-doped SnO_2 than that of SnO_2 (>486.4 eV) is due to the presence of oxygen deficiency.[45, 46] Fig. 3c shows the high resolution XPS spectrum of oxygen. The shape of a wide peak indicates that there exist several chemical bonding state according to the value of binding energy. It is related to oxygen-metal bonding of $O_{Ti\text{-}O}$ and $O_{Sn\text{-}O}$, C–O or C=O bonding, and adsorbed water with increased binding energy, which are denoted as O_{I}, O_{II}, O_{III}, respectively. Using the XPS Peak fitting program, version 4.1, each O 1s XPS spectrum is fitted to three peaks centered at 530.5, 532.4, and 533.2eV. The peak at lower binding energy of 530.5 eV can be attributed to oxygen of Ti-SnO_2, while the peak centered at 532.4 eV is due to the the oxygen in C–O or C=O bounds.[47] The peak at 533.2 eV should be ascribed to adsorbed water, the intensity of which is much lower than the others.[48] The XPS spectrum in Fig. 3b shows that the binding energy of Ti 2P$_{3/2}$ and Ti 2P$_{1/2}$ peak is 464.6 and 458.5eV, respectively, indicating Ti is doped into lattice of SnO_2 in the form of Ti^{4+}, in agreement with the reported literature values.[49, 50] The additional broad peak at 472 eV in the Ti 2p XPS spectra is known satellite peak from Ti 2p, which is related to the existence of Plasmons. Similar phenomenon can be observed in other previous work on Sn-doped titania photocatalysts.[51] The shoulder peak around 497 eV in the Sn 3d region might be similarly ascribed to the satellites, or a signal noise.

The microstructure and surface morphology of pure SnO_2 and Ti-doped SnO_2 samples were characterized using a SU-70 field-emission scanning electron microscope (FESEM), as shown in Fig. 4. As can be seen from Fig. 4a, the prepared SiO_2 spherical samples display an average size of 300 nm and are relatively monodisperse. As depicted in low- and high-magnification FESEM images in Fig. 4b-4c for pure SnO_2 sample synthesized using SiO_2 spheres as templates, the SnO_2 spherical products display hollow structural characteristics with an average of 300 nm similar to that of SiO_2 templates. The morphology and size of the hollow structured SnO_2 spheres are uniquely distributed. Fig. 4d-4f shows low-magnification FESEM images of the Ti-doped SnO_2 materials with 10, 20, 50 mol% Ti doping contents. It clearly indicates that the addition of Ti does not destroy the structure and surface morphology of Ti-doped SnO_2 products, and still exhibit macroporous spherical structure with size of approximately 300 nm. The elemental energy-dispersive spectroscopy (EDS) mapping characterization was carried out to further describe the microstructures on chemical composition and element distribution of the as-synthesized SnO_2 (20%Ti) (Fig. S1), showing that SnO_2 (20%Ti) sample is composed of Sn, O and Ti elements, Sn, O and Ti elementals (Fig. S1b-1d, Fig. S2) are homogeneously distributed among the sample.

Transmission electron microscopy (TEM) was used to further characterize the microstructure of SnO_2 (20%Ti) sample, as is shown in Fig. 5. From the low magnification TEM images in Fig. 4a-4b, it is shown that the diameter of hollow structured 20%Ti-doped SnO_2 is about 300 nm, which is coincident with that obtained from SEM analysis. A high-resolution TEM lattice image in Fig. 5c suggests that the Ti-doped SnO_2 is composed of fine nanoparticles with an average diameter of 5-6 nm. It is obviously shown that the Ti-doped SnO_2 sample is highly crystalline. The crystal structural nature of the samples is determined according to the selected area electron diffraction (SAED) analysis in Fig. 5d, revealing a polycrystalline nature of the as-synthesized tetragonal rutile SnO_2 (space group: *P42/m*) with lattice constants of a = 4.74 Å , c = 3.19 Å. The diffraction rings in Fig. 5d correspond well with that of the (110), (101), (200), (220), (202) planes of tetragonal rutile SnO_2. **Fig. 6**a depicts a high resolution TEM lattice image taken along [534] zone axis. The marked d-spacing of 0.15 nm and 0.14 nm correspond well to that of (2-2-1) and (11-2) planes of tetragonal SnO_2. Fig. 6b gives atypical HRTEM lattice image taken along [214] zone axis. The marked d-spacing of 0.21 nm and 0.19 nm correspond well to that of (-120) and (-201) planes of tetragonal SnO_2..

3. 2 UV-vis absorption properties of hollow structured Ti- doped SnO_2 photocatalyst

Fig. 7a shows the UV-vis absorption spectra of ethanol solution mixed with hollow structured Ti-doped SnO_2 with different Ti doping levels. The UV-vis spectrum of pure SnO_2 shows a strong peak at 250 nm, which is attributed to the electronic transition from the valence band (VB) to the conduction band (CB) of SnO_2. When dopants and defects are introduced, additional extrinsic electronic levels can be located in the energy band gap of the SnO_2. It can be seen that both pure SnO_2 and Ti-doped SnO_2 show obvious UV-light absorption. As compared to the UV-vis spectrum of pure SnO_2, the absorption edges of SnO_2 with different Ti doping contents shift red gradually. Especially, it's worthwhile to note that the UV-vis spectrum of the Ti-doped SnO_2 extends into the visible light region due to the incorporation of Ti dopants into lattice of SnO_2. The shifting of optical absorption edge of Ti-doped SnO_2 to the lower energy region, extending into visible light region is mainly attributed to the narrowed band gap caused by the evolution of the electronic structure.

In order to investigate the influence of doping concentrations on the optical band gap, the band gap energy of the Ti-doped SnO_2 samples can be calculated roughly according to the plots in Fig. 6b, which is obtained via the transformation based on the following formula:

$$(\alpha h\nu)^2 = K(h\nu - Eg),$$

where α is the absorbance, hν is the photon energy, and K is the parameter. The estimated band gap values of SnO_2, 10%, 20%, 50% Ti-doped SnO_2 correspond approximately to the light responsibility with an energy band gap of 3.65, 3.08, 3.32, 3.45 eV, respectively (Fig. 7b), as illustrated in Table 4. Therefore, it can be concluded that the transition of light responsibility from UV to visible light of Ti-doped SnO_2 samples can be realized by homogeneous doping in SnO_2.

Table 4 The band gap of SnO_2 with different Ti doping concentration levels

Sample	SnO_2	SnO_2(10%Ti)	SnO_2(20%Ti)	SnO_2(50%Ti)
Band gap	3.65	3.32	3.02	3.45

3. 3 Photocatalytic activity of hollow structured Ti-doped SnO_2 photocatalysts

Photocatalytic activity of Ti-doped SnO_2 and pure SnO_2 photocatalysts are comparatively investigated by decomposing a representative Methylene Blue (MB) organic pollutant under UV and visible light irradiation, respectively. The time-dependent UV-Vis spectra of an aqueous MB solution in the presence of Ti-doped SnO_2 photocatalysts under UV and visible light irradiation for regular time intervals are displayed in Fig. S3-S4, respectively. It is indicated that the intensity of absorption peaks for MB decreases gradually with the reaction time increasing under UV and visible light irradiation. When illuminated by UV and visible light, the Ti-doped SnO_2 photocatalysts display much higher photocatalytic efficiency than pure SnO_2 due to the homogeneous Ti doping effect.

The degradation efficiency of the hollow SnO_2 and Ti-doped SnO_2 nanostructures under UV and visible light irradiation is defined as C/C_0, where C_0 and C are the initial and instantaneous concentration of MB, respectively. Fig. 8a depicts the photocatalytic activity of the as-prepared photocatalysts under UV light. It is found that Ti-doped SnO_2 specimens display enhanced photocatalytic activity on MB than SnO_2 samples. Especially, Ti-doped SnO_2 with a doping content of 20 mol% can photocatalytically degrade 92% MB within degradation time of 135 min under the irradiation of UV (Fig. 8a). Also, 54% MB can be photocatalytically decomposed in the presence of 20%Ti-doped SnO_2 hollow structured sample within degradation time of 135 min under the irradiation of visible light (Fig. 8b). According to previous studies,[52,53] the degradation of dyes can be ascribed to a pseudo-first-orderreaction with a simplified Langmuir–Hinshelwood model when C_0 is very small: $\ln(C_0/C) = kt$, where k is the apparent first-order rate constant. As displayed in Fig. 9a, 20%Ti-doped SnO_2 hollow structured sample displays the highest rate constant (ca. 0.01507 min^{-1}) among all the samples under the irradiation of UV light. The photocatalytic activity and the kinetic rate constants of the Ti-doped SnO_2 hollow structured photocatalysts with different Ti loading follow the order: SnO_2 (20%Ti) > SnO_2 (10%Ti) > SnO_2 (50%Ti) > SnO_2. Also, the photocatalytic activity was explored under the irradiation of visible light, and the similar behavior of photocatalytic activity can be observed. As shown in Fig. 9b, both the Ti-doped SnO_2 hollow structured photocatalysts show enhanced photocatalytic activity compared to the pure SnO_2, the SnO_2 (20%Ti) sample still shows the best photocatalytic activity, the kinetic rate constants of the Ti-doped SnO_2 hollow structured photocatalysts with different Ti loading follow the order: SnO_2 (20%Ti) > SnO_2 (10%Ti) > SnO_2 (50%Ti) > SnO_2.

For the Ti-doped SnO_2 photocatalysts, the photocatalytic activity increase with the Ti^{4+} doping concentration increasing, as the Ti doping content is below 20 mol%. There exists an optimal doping Ti content of 20 mol% for the best photoctalytic activity toward decomposing MB both under UV and visible irradiation for the Ti-doped SnO_2 hollow structured photocatalysts. As the Ti doping content is higher than the optimal value of 20 mol%, Ti doping becomes detrimental for the photocatalytic activity. At lower doping concentration below the optimal value, photocatalytic activity increases with dopant content increasing, because there are fewer trapping sites available, the existence of an optimal Ti dopant concentration in SnO_2 matrix can be expound by the balance of an increase in trapping sites bringing about efficient trapping and fewer trapped carriers bringing about longer lifetimes for interfacial charge transfer.[54,55] The detailed mechanism will be discussed in the next section.

3. 4 Mechanism of photocatalytic activity enhancement of Ti-doped SnO_2

The relevant mechanism related to the photocatalytic performance enhancement of Ti-doped SnO_2 can be attributed to the following reasons. Homogenous doping of Ti into lattice of SnO_2 prevents the recombination of the electron-hole pairs, and expands the range of useful excitation light to the visible light region (Fig. 10). In addition, the small size of Ti-SnO_2 nanoparticles, highly crystalline state, large surface area, and large pore size of the Ti-doped SnO_2 also contribute to the improved photocatalytic activity of the Ti-doped SnO_2 samples.

Under light irradiation, SnO_2 samples absorb the light photons. As the absorbed photon energy is larger than the band gap of SnO_2, electrons are excited from the valence band (VB) to the conduction band (CB), creating electron-hole pairs. These charge carriers migrate to the surface and react with MB molecules absorbed on the surface. However, during the migration process, many electrons and holes may recombine, and as a result the charge recombination may decrease the photocatalysis efficiency. Furthermore, since the optical response of SnO_2 is limited to UV light region due to its inherently band gap energy of 3.62 eV, its photocatalytic application is restricted only to the UV range. One of the potential solutions for improving photocatalytic efficiency of SnO_2 is to shift its absorption from the UV region to the visible-light region and efficiently decrease the recombination rate of photogenerated charges, allowing for more photons to be absorbed and utilized in decomposing the pollutants.

It has been widely recognized that the photocatalytic efficiency of semiconductor oxide materials can be improved substantially by introduction of metallic ions owing to modification of their band-gap energy structures and introduction of dopant energy states. In the present work, the above microstructure and UV-vis spetra analysis have shown that Ti homogeneously doping can shift the absorption edge of SnO_2 to the visible light range and narrow the band gap of SnO_2. It is shown that there exists an optimal doping concentration of 20 mol% Ti for Ti-doped SnO_2 to photocatalytically decompose 92% MB within 135 min under UV light, and 54% MB within 135 min under visible light, respectively.

Substitution of Sn^{4+} by Ti ions in the SnO_2 lattice creates allowed energy states in the band gap of SnO_2, generating photoactive transitions due to excitation of an electron from this energy level to the SnO_2 conduction band (CB). Ti doping influences the photoreactivity of SnO_2 by acting as electron traps and by altering the electron-hole pair recombination rate. According to the schematic diagram for photocatalytic mechanism of Ti-doped SnO_2 photocatalysts shown in Fig. 10, the hypothetical process proposed for the photocatalytic degradation of MB is as follows:

$$SnO_2 + h\nu \rightarrow SnO_2\,(e_{CB}^{-} + h_{VB}^{+}) \tag{1}$$

$$e_{CB}^{-} + O_2 \rightarrow \bullet O_2^{-} \tag{2}$$

$$\bullet O_2^{-} + H^{+} \rightarrow \bullet HO_2 \tag{3}$$

$$\bullet HO_2 + e_{CB}^{-} + H^{+} \rightarrow H_2O_2 \tag{4}$$

$$H_2O_2 + e_{CB}^{-}/\bullet O_2^{-} \rightarrow \bullet OH + OH^{-} \tag{5}$$

$$h_{VB}^{+} + H_2O \rightarrow \bullet OH + H^{+} \tag{6}$$

$$h_{VB}^{+} + OH^{-} \rightarrow \bullet OH \tag{7}$$

$$\cdot OH + MB \rightarrow \text{Degradation products} \tag{8}$$

The photogenerated electrons can be scavenged by dissolved oxygen molecules (O_2) on or near the photocatalyst surface to produce a superoxide anion radical (•O_2^-) and hydrogen peroxide (H_2O_2). The formed •O_2^- might either directly oxidize MB or yield hydroxyl radicals (•OH) by reacting with hydrion (H^+) and photogenerated electrons (e_{CB}^-). The photoinduced holes (h_{VB}^+) in the valence band can be trapped by OH^- or H_2O species adsorbed on the surface of the catalyst, to further generate reactive •OH species, which is an extremely strong oxidizing agent for the partial or complete decomposition of MB molecules.

In the case for the Ti dopant concentration lower than 20 mol%, the Ti doping is helpful to trap photogenerated electrons so as to limit the charge recombination, which is one of the main factors in determining the photocatalytic activity of SnO_2. The space-charge region becomes narrower with the increasing of Ti dopant concentration, and therefore the electron-hole pairs are efficiently prevented from recombination by the large electric field. Nevertheless, too high-loading concentration of Ti would be utilized as recombination centers for electron-hole pairs. As the concentration of doping is higher than a threshold level, the space-charge region becomes so narrow that the light penetration depth greatly exceeds the space-charge layer. The recombination of photogenerated electron-hole pairs in the semiconductor thus increases because there is no driving force to realize the separation of electron-hole pairs. Hence, there exists an optimum concentration of Ti dopant to guarantee that the thickness of light penetration depth is approximately equivalent to the space charge layer. As a consequence, the recombination rate increases significantly with the dopant concentration increasing above the threshold level of Ti doping concentration. Therefore, as observed and confirmed in the present work, an optimum Ti-doped content is required to optimize its role of photogenerated electron trapping. It is shown that as the Ti loading content is higher than the optimal value of 20 mol%, the higher content doping of Ti^{4+} becomes detrimental for the photocatalytic activity. Furthermore, due to the lower band gap energy, the light absorption capacity of the Ti-doped SnO_2 samples is higher than that of pure SnO_2. It can efficiently utilize solar energy in the visible light region and result in the generation of more e- and h+ pairs, thus enhancing the photocatalytic activity of Ti-SnO_2 catalyst toward decomposing MB pollutants.

Photocatalytic activity is closely associated with the lifetime of photogenerated electrons and holes. It is generally accepted that PL signals result from the recombination of photoinduced charge carriers. PL emission spectra of hollow structured Ti-doped SnO_2 with different Ti doping concentration are used to describe the recombination rate of photoexcited electrons and holes, as presented in Fig. 11. It is shown that all Ti-doped SnO_2 samples exhibit lower PL emission intensity than pure SnO_2 sample, indicating that the recombination of photoexcited electrons and holes of Ti-doped SnO_2 photocatalyst is efficiently hindered, thus successfully effectively implementing the separation of electrons and holes. The efficient separation of electron–hole pairs is exactly advantageous to the enhancement of photocatalytic activity of Ti-doped SnO_2. At the relative low Ti loading content, along with the increment of Ti doping concentration, the recombination of photoexcite electron–hole pairs is restricted effectively, nevertheless. As the Ti doping content is higher than the optimal value of 20 mol %, the relevant recombination rate of photoexcited electron–hole pairs contrarily exhibits a increasing trend. As a consequence, the photocatalytic activity should comply with such a regularity described that the 20% Ti-doped SnO_2 shows the best photocatalytic performance toward decomposing the MB pollutants.

The enhanced photocatalytic activity can also be attributed to unique structural characteristics of hollow Ti-doped SnO_2. It is shown that the silica-template synthesized hollow structured 20%Ti-SnO_2 samples display high surface area (35.6±0.5 m^2 g^{-1}), large volume (0.54 cm^3 g^{-1}), pore size (0.61 ± 0.01 nm), accordingly, the 20%Ti-SnO_2 sample possesses the higher rate constants than pure SnO_2 and thus shows the enhanced photocatalytic activity. Furthermore, the incorporation of Ti species into lattice of SnO_2 induces the grain refinement of SnO_2. According to TEM analysis, the average particle size of Ti-doped SnO_2 (20Ti %) can be calculated to be 6 nm, and the Ti-doped SnO_2 samples are highly crystalline. The fine particle size, highly crystalline, large surface area and porous structure contribute to a higher photocatalytic performance for the Ti-doped SnO_2 samples.[56, 57]

4 Conclusions

A facile infiltration route is developed to prepare hollow structured Ti-doped SnO_2, using silica microspheres as the templates, stannous chloride as the tin precursor, tetrabutyl titanate as the titanium precursor. The microstructures and chemical compositions of Ti-doped SnO_2 samples were characterized by XRD, XPS, BET, SEM and TEM. XRD and SEM results reveal that the crystal structure and morphology is not affected by Ti doping, maintaining a highly crystalline state and hollow spherical nanostructure with a diameter of about 300 nm. Ti is uniformly incorporated into lattice of SnO_2 materials in the form of Ti^{4+}. Ti doping into lattice of SnO_2 increases the BET surface area from 26.2±0.5 m^2 g^{-1} of SnO_2 to 35.6±0.5 m^2 g^{-1} of SnO_2 (20%Ti), effectively induces light response transition from UV region to visible region and greatly inhibits the recombination of electron-hole pairs on SnO_2, which play essential roles in improving the photocatalytic activity of Ti-doped SnO_2. The photocatalytic activity of the hollow structured Ti-doped SnO_2 photocatalysts was investigated by decomposing Methylene Blue (MB) under UV and visible light illumination in a photochemical reactor. It is revealed that the hollow structured Ti-doped SnO_2 spherical specimens display enhanced photocatalytic activity toward decomposing MB than pure SnO_2 sample. The relation between microstructure, optical responsibility, photocatalytic performance is discussed and analyzed. The mechanism related to photocatalytic performance enhancement of Ti-doped SnO_2 is systematically investigated.

Acknowledgment

We acknowledge support from the National Natural Science Funds for Distinguished Young Scholars (No.: 51025211), National Nature Science Foundation of China (No.: 51472148, 51272137), the Tai Shan Scholar Foundation of Shandong Province.

References

(1) Carey, J.; Lawrence, J.; Tosine, H., Photodechlorination of PCB's in the Presence of Titanium Dioxide in Aqueous Suspensions. *Bull. Environ. Contam. Toxicol.* **1976,** *16* (6), 697-701.

(2) Frank, S. N.; Bard, A. J., Heterogeneous Photocatalytic Oxidation of Cyanide and Sulfite in Aqueous Solutions at Semiconductor Powders. *J. Phys. Chem.* **1977,** *81* (15), 1484-1488.

(3) Vinodgopal, K.; Bedja, I.; Kamat, P. V., Nanostructured Semiconductor Films for Photocatalysis. Photoelectrochemical Behavior of SnO_2/TiO_2 Composite Systems and Its Role in Photocatalytic Degradation of a Textile Azo Dye. *Chem. Mater.* **1996,** *8* (8), 2180-2187.

(4) Garwin, L.; Ball, P., Science at the Atomic Scale. *Nature* **1992,** *355* (6363), 761.

(5) Halperin, W., Quantum Size Effects in Metal Particles. *Rev. Mod. Phys.* **1986,** *58* (3), 533-606.

(6) Fujishima, A.; Rao, T. N.; Tryk, D. A., TiO_2 Photocatalysts and Diamond Electrodes. *Electrochim. Acta* **2000,** *45* (28),

4683-4690.

(7) Hoffmann, M. R.; Martin, S. T.; Choi, W.; Bahnemann, D. W., Environmental Applications of Semiconductor Photocatalysis. *Chem. Rev.* **1995,** *95* (1), 69-96.

(8) Tachikawa, T.; Fujitsuka, M.; Majima, T., Mechanistic Insight into the TiO_2 Photocatalytic Reactions: Design of New Photocatalysts. *J. Phys. Chem. C* 2007, *111* (14), 5259-5275.

(9) a) Nayral, C.; Ould-Ely, T.; Maisonnat, A.; Chaudret, B.; Fau, P.; Lescouzères, L.; Peyre-Lavigne, A., A Novel Mechanism for the Synthesis of Tin /Tin Oxide Nanoparticles of Low Size Dispersion and of Nanostructured SnO_2 for the Sensitive Layers of Gas Sensors. *Adv. Mater.* **1999,** *11* (1), 61-63; b) Renard, L.; Babot, O.; Saadaoui, H.; Fuess, H.; Brotz, J.; Gurlo, A.; Arveux, E.; Klein, A.; Toupance, T., Nanoscaled tin dioxide films processed from organotin-based hybrid materials: an organometallic route toward metal oxide gas sensors. *Nanoscale* **2012,** *4* (21), 6806-6813; c) Renard, L.; Brotz, J.; Fuess, H.; Gurlo, A.; Riedel, R.; Toupance, T., Hybrid organotin and tin oxide-based thin films processed from alkynylorganotins: synthesis, characterization, and gas sensing properties. *ACS Appl. Mater. Inter.* **2014,** *6* (19), 17093-101.

(10) a) Lou, X. W.; Li, C. M.; Archer, L. A., Designed Synthesis of Coaxial SnO_2@carbon Hollow Nanospheres for Highly Reversible Lithium Storage. *Adv. Mater.* **2009,** *21* (24), 2536-2539; b) Liu, J.; Xue, D., Hollow Nanostructured Anode Materials for Li-Ion Batteries. *Nanoscale Res. Lett.* **2010,** *5* (10), 1525-1534; c) Liu, J.; Xia, H.; Xue, D.; Lu, L., Double-Shelled Nanocapsules of V_2O_5-Based Composites as High-Performance Anode and Cathode Materials for Li Ion Batteries. *J. Am. Chem. Soc.* **2009,** *131* (34), 12086-12087; d) Chen, J. S.; Lou, X. W.; SnO_2-Based Nanomaterials: Synthesis and Application in Lithium-Ion Batteries. *Small* **2013,** *9* (11), 1877-1893.

(11) Ginley, D. S.; Bright, C., Transparent Conducting Oxides. *MRS Bull.* **2000,** *25* (08), 15-18.

(12) a) Ferrere, S.; Zaban, A.; Gregg, B. A., Dye sensitization of Nanocrystalline Tin Oxide by Perylene Derivatives. *J. Phys. Chem. B* **1997,** *101* (23), 4490-4493; b) Cojocaru, L.; Olivier, C.; Toupance, T.; Sellier, E.; Hirsch, L., Size and shape fine-tuning of SnO_2 nanoparticles for highly efficient and stable dye-sensitized solar cells. *J. Mater. Chem. A* **2013,** *1* (44), 13789-13799; c) Kumar, E. N.; Jose, R.; Archana, P. S.; Vijila, C.; Yusoff, M. M.; Ramakrishna, S., High performance dye-sensitized solar cells with record open circuit voltage using tin oxide nanoflowers developed by electrospinning. *Energy Environ. Sci.* **2012,** *5* (1), 5401-5407.

(13) Wang, X.; Fan, H.; Ren, P., Electrospinning Derived Hollow SnO_2 Microtubes with Highly Photocatalytic Property. *Catal. Commun.* **2013,** *31* (0), 37-41.

(14) Talebian, N.; Jafarinezhad, F., Morphology-Controlled Synthesis of SnO_2 Nanostructures Using Hydrothermal Method and Their Photocatalytic Applications. *Ceram. Int.* **2013,** *39* (7), 8311-8317.

(15) Levy, B.; Liu, W.; Gilbert, S. E., Directed Photocurrents in Nanostructured TiO_2/SnO_2 Heterojunction Diodes. *J. Phys. Chem. B* **1997,** *101* (10), 1810-1816.

(16) Jia, X.; Liu, Y.; Wu, X.; Zhang, Z., A Low Temperature Situ Precipitation Route to Designing Zn-doped SnO_2 Photocatalyst with Enhanced Photocatalytic Performance. *Appl. Surf. Sci.* **2014,** *311* (0), 609-613.

(17) Li, K.; Li, Y.; Xue, D., Band Gap Engineering of Crystal Materials: Band Gap Estimation of Semiconductors via Electronegativity. *Funct. Mater. Lett.* **2012,** *05* (02), 1260002.

(18) Li, K.; Xue, D., Estimation of Electronegativity Values of Elements in Different Valence States. *J. Phys. Chem. A* **2006,**

110 (39), 11332-11337.

(19) Pan, S.; Wang, S.; Zhang, Y.; Xu, S.; Kong, F.; Luo, Y.; Tian, Y.; Teng, X.; Li, G., Surface Fe^{3+}-Decorated Pristine SnO_2 Nanoparticles with Enhanced ·OH Radical Generation Performance. *Catal. Commun.* **2012,** *24* (0), 96-99.

(20) Rashad, M. M.; Ismail, A. A.; Osama, I.; Ibrahim, I. A.; Kandil, A.-H. T., Decomposition of Methylene Blue on Transition Metals Doped SnO_2 Nanoparticles. *CLEAN – Soil, Air, Water* **2014,** *42* (5), 657-663.

(21) Lu, Y.; Wang, P.-J.; Zhang, C.-W.; Feng, X.-Y.; Jiang, L.; Zhang, G.-L., First-Principle Study on the Electronic and Optical Properties of Mn-Doped SnO_2. *Condens. Matter Phys.B* **2011,** *406* (17), 3137-3141.

(22) Kumar, V.; Govind, A.; Nagarajan, R., Optical and Photocatalytic Properties of Heavily F^--Doped SnO_2 Nanocrystals by a Novel Single-Source Precursor Approach. *Inorg. Chem.* **2011,** *50* (12), 5637-5645.

(23) Pan, S. S.; Shen, Y. D.; Teng, X. M.; Zhang, Y. X.; Li, L.; Chu, Z. Q.; Zhang, J. P.; Li, G. H.; Hu, X., Substitutional Nitrogen-Doped Tin Oxide Single Crystalline Submicrorod Arrays: Vertical Growth, Band Gap Tuning and Visible Light-Driven Photocatalysis. *Mater. Res. Bull.* **2009,** *44* (11), 2092-2098.

(24) Li, J.; Hu, W.; Zhong, J.; Zeng, J.; Huang, S.; Xiao, Z.; Li, M., Photo-Induced Charge Separation and Photocatalytic Activity of Ga-Doped SnO_2. *Appl. Phys. A* **2014,** *116* (4), 2149-2156.

(25) Vignesh, K.; Hariharan, R.; Rajarajan, M.; Suganthi, A., Photocatalytic Performance of Ag Doped SnO_2 Nanoparticles Modified with Curcumin. *Solid State Sci.* **2013,** *21* (0), 91-99.

(26) Wu, W.; Liao, L.; Zhang, S.; Zhou, J.; Xiao, X.; Ren, F.; Sun, L.; Dai, Z.; Jiang, C., Non-Centrosymmetric Au-SnO_2 Hybrid Nanostructures with Strong Localization of Plasmonic for Enhanced Photocatalysis Application. *Nanoscale* **2013,** *5* (12), 5628-5636.

(27) Chang, Y. C.; Yan, C. Y.; Wu, R. J., Preparation of Pt@ SnO_2 Core - Shell Nanoparticles for Photocatalytic Degradation of Formaldehyde. *J. Chin. Chem. Soc.* **2014,** *61* (3), 345-349.

(28) Ristić, M.; Ivanda, M.; Popović, S.; Music, S., Dependence of Nanocrystalline SnO_2 Particle Size on Synthesis Route. *J. Non-Cryst. Solids* **2002,** *303* (2), 270-280.

(29) Liu, Z.; Zhang, D.; Han, S.; Li, C.; Tang, T.; Jin, W.; Liu, X.; Lei, B.; Zhou, C., Laser Ablation Synthesis and Electron Transport Studies of Tin Oxide Nanowires. *Adv. Mater.* **2003,** *15* (20), 1754-1757.

(30) Ding, S.; Chen, J. S.; Qi, G.; Duan, X.; Wang, Z.; Giannelis, E. P.; Archer, L. A.; Lou, X. W., Formation of SnO_2 Hollow Nanospheres inside Mesoporous Silica Nanoreactors. *J. Am. Chem. Soc.***2010,** *133* (1), 21-23.

(31) Duan, J.; Yang, S.; Liu, H.; Gong, J.; Huang, H.; Zhao, X.; Zhang, R.; Du, Y., Single Crystal SnO_2 Zigzag Nanobelts. *J. Am. Chem. Soc.* **2005,** *127* (17), 6180-6181.

(32) Hu, J. Q.; Bando, Y.; Golberg, D., Self-Catalyst Growth and Optical Properties of Novel SnO_2 Fishbone-Like Nanoribbons. *Chem. Phys. Lett.* **2003,** *372* (5–6), 758-762.

(33) Cheng, B.; Russell, J. M.; Shi; Zhang, L.; Samulski, E. T., Large-Scale, Solution-Phase Growth of Single-Crystalline SnO_2 Nanorods. *J. Amer. Chem. Soc.* **2004,** *126* (19), 5972-5973.

(34) Liu, B.; Zeng, H. C., Salt-Assisted Deposition of SnO_2 on α-MoO_3 Nanorods and Fabrication of Polycrystalline SnO_2 Nanotubes. *J. Phys. Chem. B* **2004,** *108* (19), 5867-5874.

(35) Dai, Z. R.; Pan, Z. W.; Wang, Z. L., Growth and Structure Evolution of Novel Tin Oxide Diskettes. *J. Amer. Chem. Soc.*

2002, *124* (29), 8673-8680.

(36) a) Németh, J.; Dékány, I.; Süvegh, K.; Marek, T.; Klencsár, Z.; Vértes, A.; Fendler, J. H., Preparation and Structural Properties of Tin Oxide−Montmorillonite Nanocomposites. *Langmuir* **2003,** *19* (9), 3762-3769; b) Zhang, M.; Yang, H.; Liu, Y.; Xue, D.; Sun, X. Functional carbonaceous compound assisted assembling of SnO_2@C nanocomposite as a lithium storage anode material. *Sci. Adv. Mater.* **2013,** *05* (01), 37-45.

(37) Miyata, H.; Itoh, M.; Watanabe, M.; Noma, T., Preparation of Highly Ordered Mesostructured Tin Oxide Film with a Microcrystalline Framework through Vapor-Induced Liquid-Crystal Templating. *Chem. Mater.* **2003,** *15* (6), 1334-1343.

(38) Liu, J.; Liu, F.; Gao, K.; Wu, J.; Xue, D., Recent developments in the chemical synthesis of inorganic porous capsules. *J. Mater. Chem.* **2009,** *19* (34), 6073-6084.

(39) Liu, J.; Xue, D., Thermal Oxidation Strategy towards Porous Metal Oxide Hollow Architectures. *Adv. Mater.* **2008,** *20* (13), 2622-2627.

(40) Chen, K.; Song, S.; Xue, D., Chemical reaction controlled synthesis of Cu_2O hollow octahedra and core-shell structures. *CrystEngComm* **2013,** *15* (46), 10028-10033.

(41) Stöber, W.; Fink, A.; Bohn, E., Controlled Growth of Monodisperse Silica Spheres in the Micron Size Range. *J. Colloid Interface Sci.* **1968,** *26* (1), 62-69.

(42) Cao, Y.; Yang, W.; Zhang, W.; Liu, G.; Yue, P., Improved Photocatalytic Activity of Sn^{4+} Doped TiO_2 Nanoparticulate Films Prepared by Plasma-Enhanced Chemical Vapor Deposition. *New J. Chem.* **2004,** *28* (2), 218-222.

(43) Ismail, A. A.; Bahnemann, D. W., Mesoporous Titania Photocatalysts: Preparation, Characterization and Reaction Mechanisms. *Appl. Surf. Sci.* **2011,** *21* (32), 11686-11707.

(44) Zhong, J. b.; Ma, D.; He, X. y.; Li, J. z.; Chen, Y. q., Preparation, Characterization and Photocatalytic Performance of $TiO_2/Ce_xZr_{1-x}O_2$ toward the Oxidation of Gaseous Benzene. J. Mater. Chem. **2010,** *256* (9), 2859-2862.

(45) Fan, J. C. C.; Goodenough, J. B., X‐Ray Photoemission Spectroscopy Studies of Sn‐Doped Indium‐Oxide Films. *J. Appl. Phys.* **1977,** *48* (8), 3524-3531.

(46) Peng, X. S.; Meng, G. W.; Wang, X. F.; Wang, Y. W.; Zhang, J.; Liu, X.; Zhang, L. D., Synthesis of Oxygen-Deficient Indium−Tin-Oxide (ITO) Nanofibers. *Chem. Mater.* **2002,** *14* (11), 4490-4493.

(47) Liu, S.; Guo, E.; Yin, L., Tailored visible-light driven anatase TiO_2 photocatalysts based on controllable metal ion doping and ordered mesoporous structure. *J. Mater. Chem.* **2012**, *22* (11), 5031-5041.

(48) Wang, C.; Shao, C.; Zhang, X.; Liu, Y., SnO_2 Nanostructures-TiO_2 Nanofibers Heterostructures: Controlled Fabrication and High Photocatalytic Properties. *Inorg. Chem.* **2009**, *48* (15), 7261-7268.

(49) Gonbeau, D.; Guimon, C.; Pfister-Guillouzo, G.; Levasseur, A.; Meunier, G.; Dormoy, R., XPS Study of Thin Films of Titanium Oxysulfides. *Surf. Sci. Lett.* **1991,** *254* (1–3), A476.

(50) Haukka, S.; Lakomaa, E. L.; Jylha, O.; Vilhunen, J.; Hornytzkyj, S., Dispersion and Distribution of Titanium Species Bound to Silica from Titanium Tetrachloride. *Langmuir* **1993,** *9* (12), 3497-3506.

(51) Stengl, V.; Grygar, T.; Henych, J.; Kormunda, M., Hydrogen peroxide route to Sn-doped titania photocatalysts. *Chem. Cent. J.* **2012,** *6* (1), 113.

(52) Burch, R.; Breen, J. P.; Meunier, F. C., A review of the selective reduction of NOx with hydrocarbons under lean-burn conditions with non-zeolitic oxide and platinum group metal catalysts. *Appl. Catal. B: Environ* **2002,** *39* (4), 283-303.

(53) Zhang, N.; Liu, S.; Fu, X.; Xu, Y.-J., Synthesis of M@TiO_2 (M = Au, Pd, Pt) Core–Shell Nanocomposites with Tunable

Photoreactivity. *J. Phys. Chem. C* **2011**, *115* (18), 9136-9145.

(54) Choi, W.; Termin, A.; Hoffmann, M. R., The Role of Metal Ion Dopants in Quantum-Sized TiO_2: Correlation between Photoreactivity and Charge Carrier Recombination Dynamics. *J. Phys. Chem.* **1994,** *98* (51), 13669-13679.

(55) Li, X. Z.; Li, F. B.; Yang, C. L.; Ge, W. K., Photocatalytic Activity of WO_x-TiO_2 under Visible Light Irradiation. *J. Photochem. Photobiol., A: Chem.* **2001,** *141* (2–3), 209-217.

(56) Ohko, Y.; Fujishima, A.; Hashimoto, K., Kinetic Analysis of the Photocatalytic Degradation of Gas-Phase 2-Propanol under Mass Transport-Limited Conditions with a TiO_2 Film Photocatalyst. *J. Phys. Chem. B* **1998,** *102* (10), 1724-1729.

(57) Song, X.; Gao, L., Fabrication of Hollow Hybrid Microspheres Coated with Silica/Titania via Sol−Gel Process and Enhanced Photocatalytic Activities. *J. Phys. Chem. C* **2007,** *111* (23), 8180-8187.

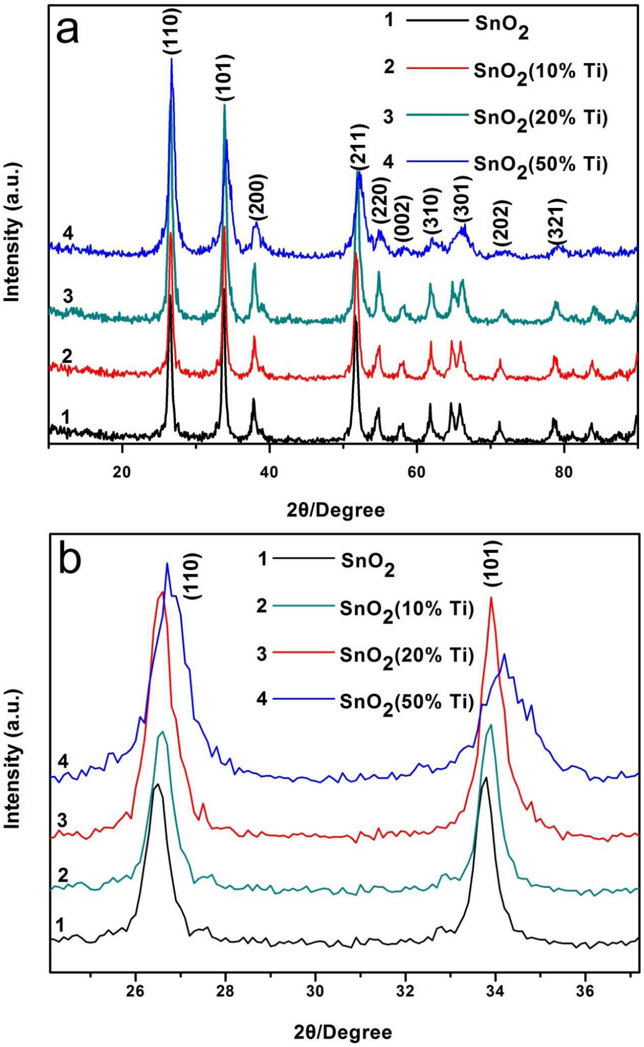

Fig. 1 (a) Wide-angle XRD patterns and (b) magnified (110) and (101) XRD peak of Ti-doped SnO$_2$ samples.

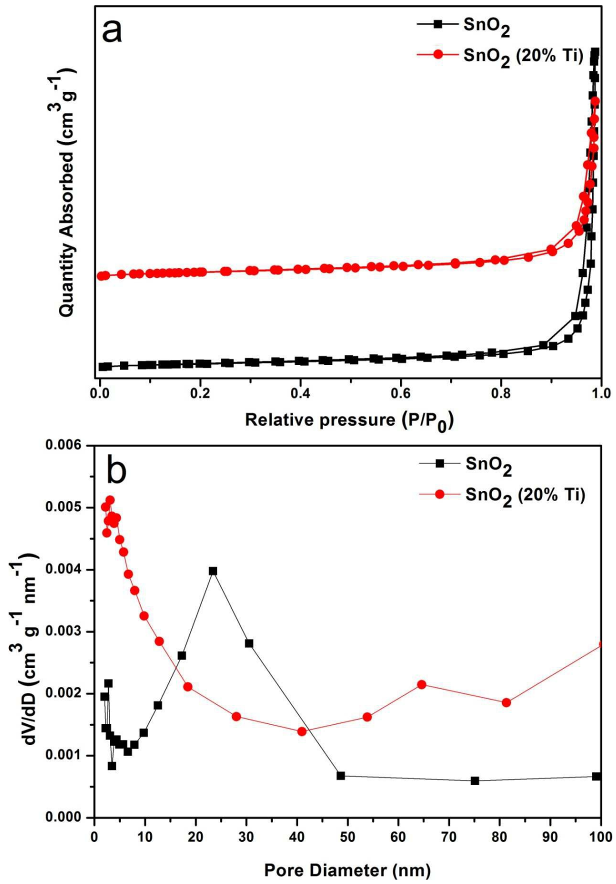

Fig. 2 (a) N_2 adsorption-desorption isotherms and (b) pore size distributions of SnO_2 and 20%Ti-doped SnO_2.

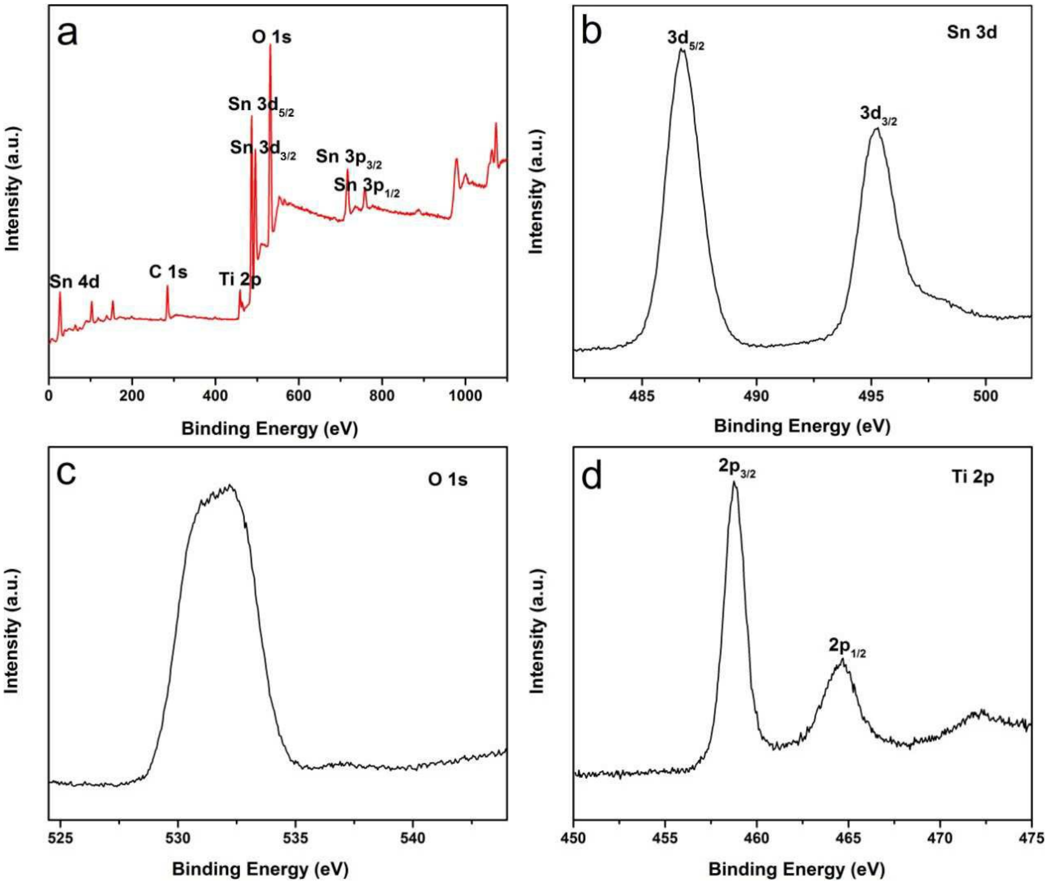

Fig. 3 XPS spectra of 20%Ti-doped SnO_2 sample. (a) Survey spectrum, (b) Ti 2p, (c) Sn 3d, (d) O 1s.

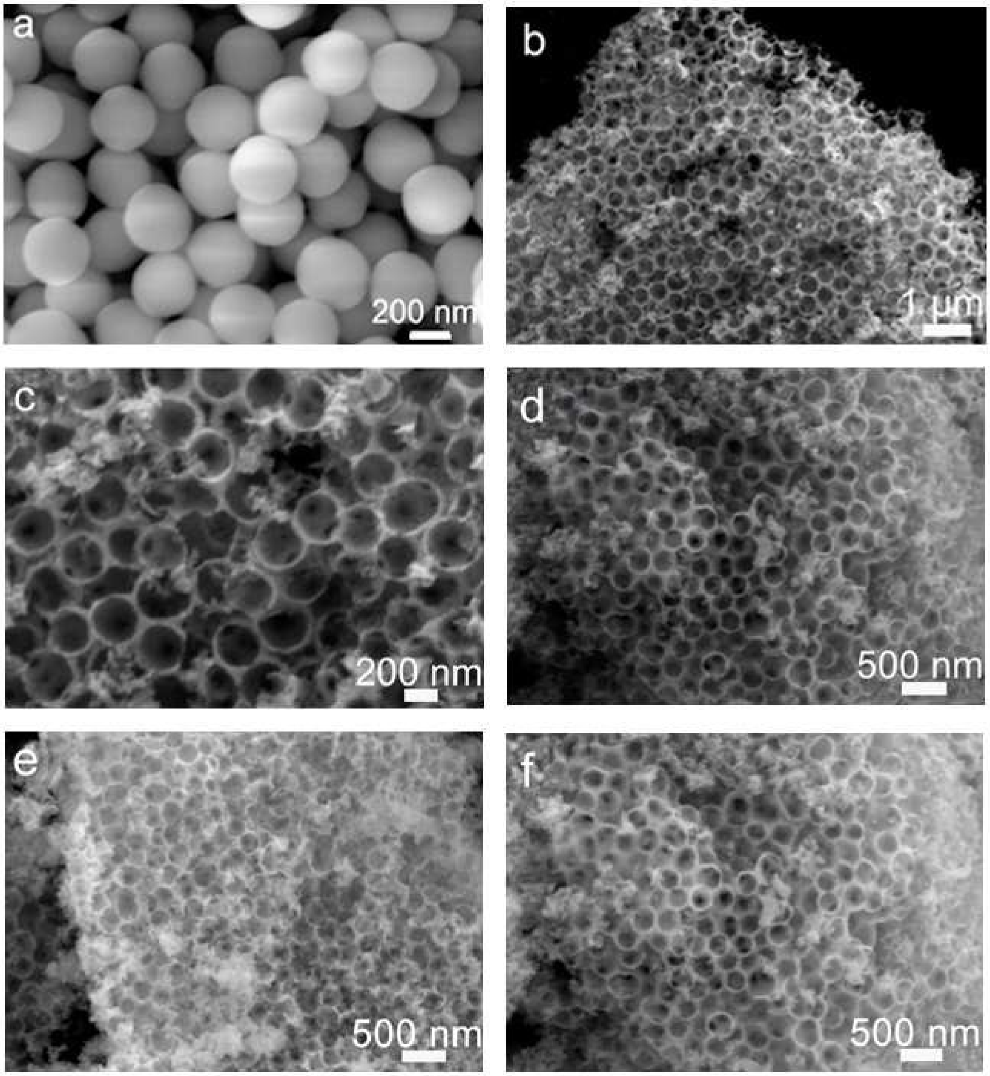

Fig. 4 SEM images of (a) SiO_2, (b) (c) SnO_2, (d) 10%Ti-doped SnO_2, (e) 20%Ti-doped SnO_2, (f) 50%Ti-doped SnO_2 samples.

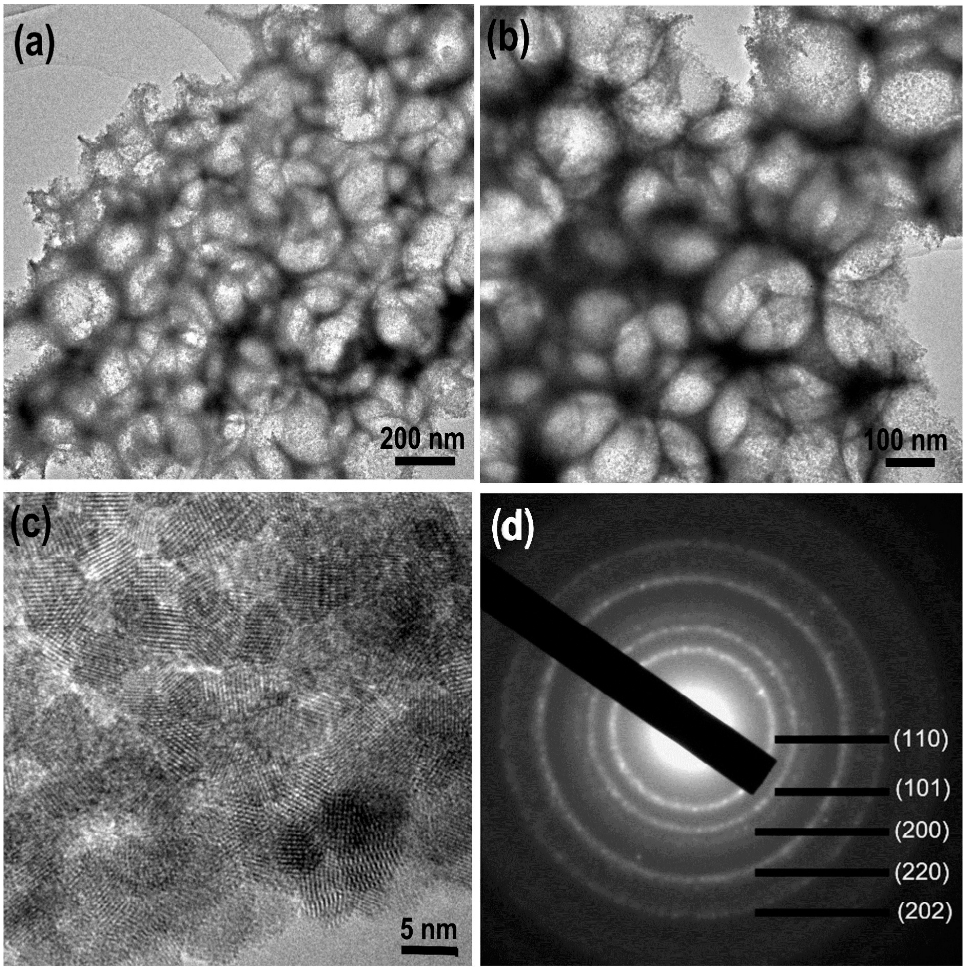

Fig. 5 (a) (b) Low magnification TEM images of 20%Ti-doped SnO_2. (c) A typical high resolution TEM lattice image of 20%Ti-doped SnO_2 shows that sample is composed of highly-crystalline nanoparticles with an average of 6 nm. (d) Selected area electron diffraction pattern of 20%Ti-doped SnO_2, the diffraction rings correspond well with that of the (110), (101), (200), (220), (202) planes of tetragonal rutile SnO_2.

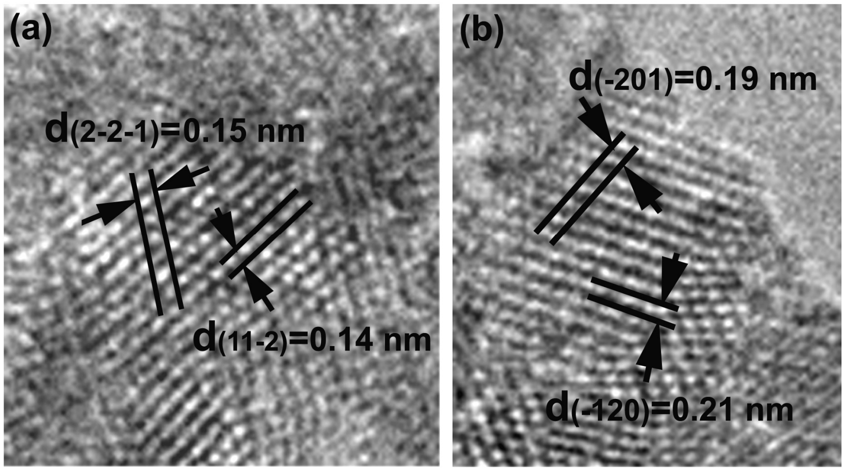

Fig. 6 (a) High resolution TEM lattice image taken along [534] zone axis. The marked d-spacing of 0.15 nm and 0.14 nm correspond well to that of (2-2-1) and (11-2) planes of tetragonal SnO_2. (b) High resolution TEM lattice image taken along [214] zone axis. The marked d-spacing of 0.21 nm and 0.19 nm correspond well to that of (-120) and (-201) planes of tetragonal SnO_2.

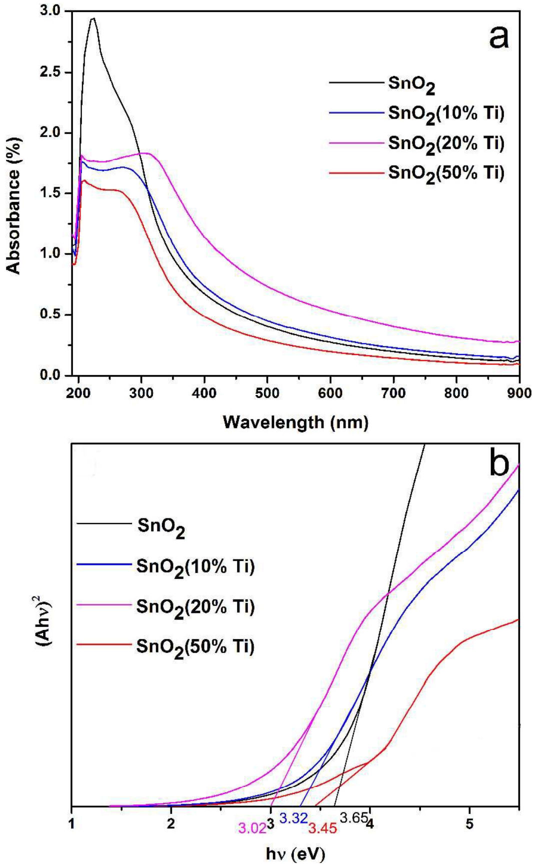

Fig. 7 (a) UV-vis spectrum of pure and SnO_2 with different Ti content doping levels. (b) $(\alpha h\nu)^2$-hν curves of pure and SnO_2 with different Ti content doping levels.

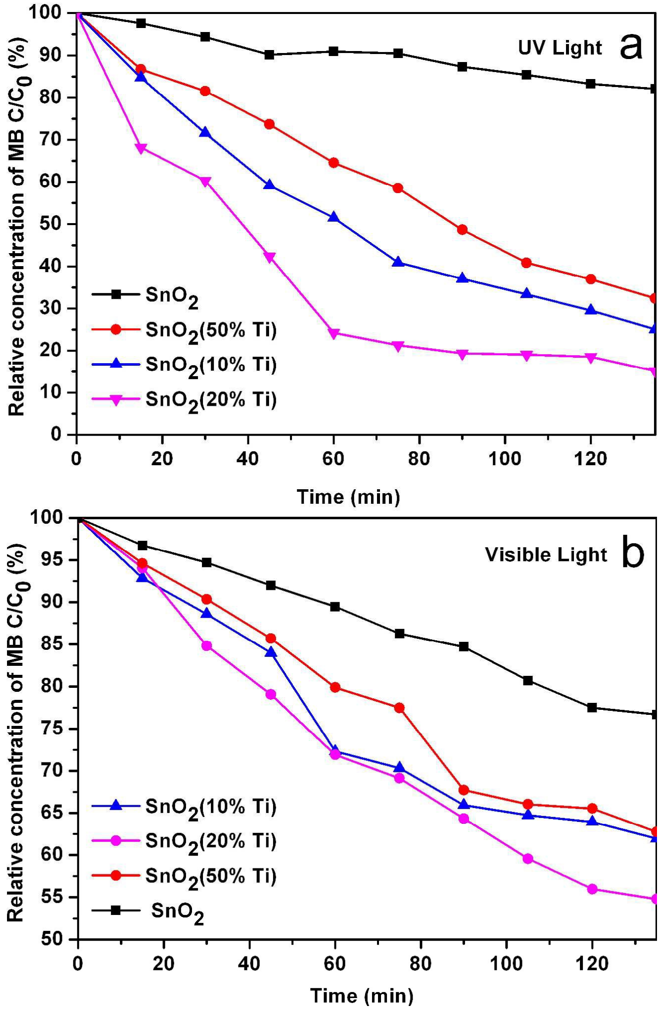

Fig. 8 Plots of (C/C_0) versus irradiation time (t) for Ti-doped SnO_2 samples under (a) UV light and (b) visible light.

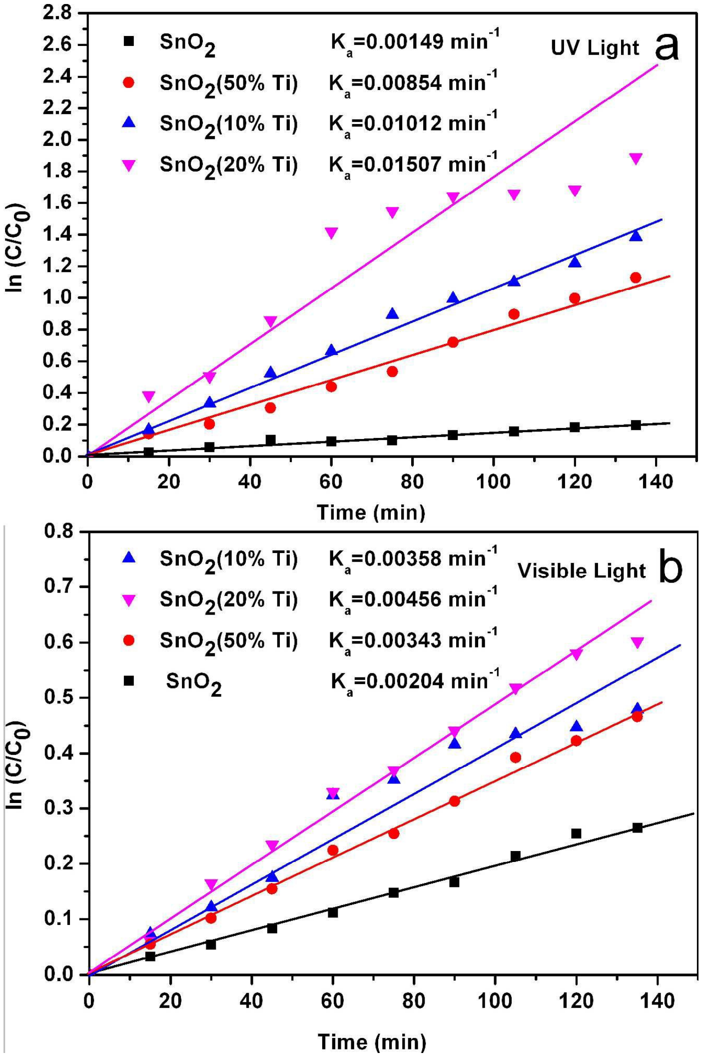

Fig. 9 Plots of ln (C/C_0) versus irradiation time (t) for Ti-doped SnO_2 samples under (a) UV light and (b) visible light.

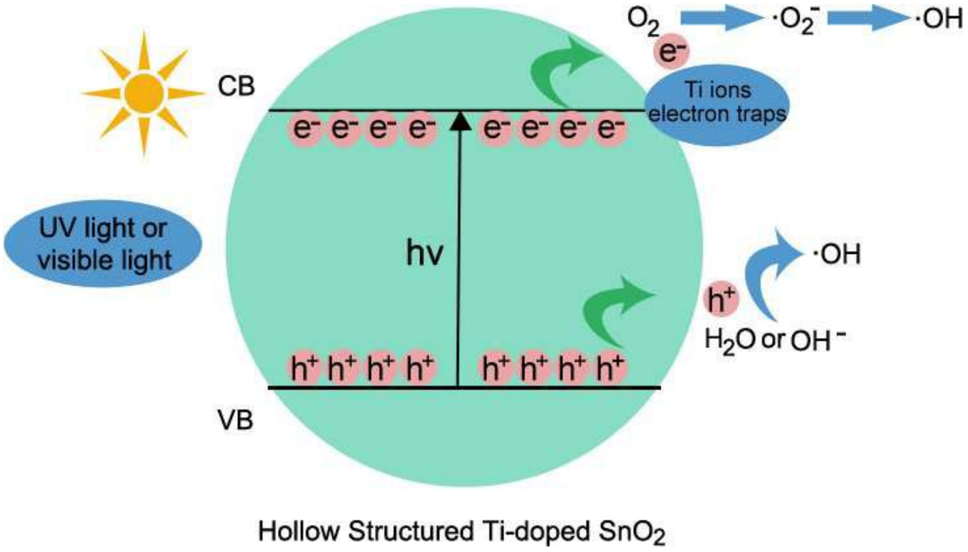

Fig. 10 The schematic diagram for photocatalytic mechanism of Ti-doped SnO_2 photocatalysts.

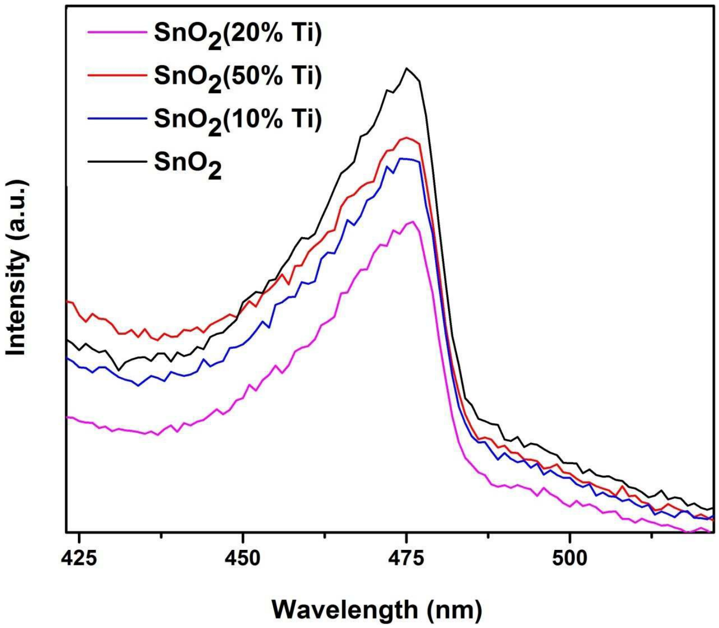

Fig. 11 PL spectra of pure and SnO_2 with different Ti content doping levels.